Junkai Ren, Luigi Stagi, Carlo Maria Carbonaro, Luca Malfatti, Maria Francesca Casula, Pier Carlo Ricci, Antonio Esau Del Rio Castillo, Francesco Bonaccorso, Laura Calvillo, Gaetano Granozzi, and Plinio Innocenzi

Defect-assisted photoluminescence in hexagonal boron nitride nanosheets

2D Mater. (2020), Volume 7, 045023

10.1088/2053-1583/ababf0

Defect-assisted photoluminescence in hexagonal boron nitride nanosheets

Junkai Ren[1], Luigi Stagi[1], Carlo Maria Carbonaro[2], Luca Malfatti[1], Maria Francesca Casula[3], Pier Carlo Ricci[2], Antonio Esau Del Rio Castillo[4], Francesco Bonaccorso[4], Laura Calvillo[5], Gaetano Granozzi[5], and Plinio Innocenzi[1]*

[1] Department of Chemistry and Pharmacy, Laboratory of Materials Science and Nanotechnology, CR-INSTM, University of Sassari, Via Vienna 2, 07100, Sassari, Italy

[2] Department of Physics, University of Cagliari, sp 8, km 0.700, 09042 Monserrato, Italy

[3] DIMCM-Department of Mechanical, Chemical, and Materials Engineering, INSTM, University of Cagliari, Via Marengo 2, 09123 Cagliari, Italy

[4] Bedimensional S.p.A. Genova, Italy and Istituto Italiano di Tecnologia, Genova, Italy

[5] Department of Chemical Sciences, University of Padua, Via Marzolo 1, 35131 Padova, Italy

*Corresponding author: plinio@uniss.it

Keywords: Hexagonal boron nitride, 2D materials, photoluminescence

Abstract

The development of functional optoelectronic applications based on hexagonal boron nitride nanosheets (*h*-BNNs) relies on controlling the structural defects. The fluorescent emission, in particular, has been observed to depend on vacancies and substitutional defects. In the present work, few-layer *h*-BNNs have been obtained by sonication-assisted liquid-phase exfoliation of their bulk counterpart. The as-prepared samples exhibit a weak fluorescent emission in the visible range, centred around 400 nm. Tailored defects have been introduced by oxidation in air at different temperatures. A significant increase in the fluorescent emission of the oxidated *h*-BNNs has been observed with maximum emissive intensity for the samples treated at 300°C. A further increase in temperatures (>300°C) determines a quenching of the fluorescence.

We investigated, by means of detailed microscopic and spectroscopic analysis, the relationship between the optical properties and defects of *h*-BNNs. The investigation of the optical properties as a function of treatment temperature highlights the critical role of hydroxyl groups created by the oxidation process. Only *h*-BN exfoliated in water allows introducing OH groups with consequent enhancement of fluorescence emission. Quantum chemical calculations support the experimental findings.

1. Introduction

Hexagonal boron nitride (*h*-BN) is a two-dimensional (2D) material in the spotlight since the isolation of graphene[1]. The wide bandgap (E_g), around 6 eV[2,3], whose

value has been confirmed by both theoretical and experimental works, has attracted much attention because of the potential applications in photonics and optoelectronic [4–7]. In addition to the remarkable ultraviolet emission, with potential applications as deep UV LED and laser[8,9], room temperature photoluminescence (PL) in the visible range has also stimulated special interests[10]. In general, the *h*-BN fluorescent quantum dots and 2D materials[11] contain multiple defects concurrently, such as the presence of carbon, oxygen and hydrogen impurities[12]. The luminescent properties of *h*-BN systems have been mainly attributed to the presence of defect states, including boron/nitrogen vacancies, carbene structure, and oxygen-doping[13,14]. However, the simultaneous presence of specific impurities or heterogeneous distribution of defects makes the comprehension of the fluorescence properties a quite difficult task. In particular, controlling the defects in 2D *h*-BN nanosheets (*h*-BNNs) is of paramount importance for the photonics and optoelectronic applications of this class of materials[15].

Fluorescent *h*-BNNs have been synthesized via both top-down and bottom-up approches[11,16]. The 2D materials produced by bottom-up synthesis, besides the structural B-N units, can also contain carbon/oxygen defects, depending on the precursors and the synthesis chemical environment[17]. Additionally, boron or nitrogen vacancies in the layered structure are common defects, which cannot be completely avoided.

Among top-down methods, ultrasonic-assisted liquid-phase exfoliation (LPE) is a straightforward route to obtain *h*-BN nanosheets. By using water as liquid, *h*-BNNs with single or few layers can be produced[18]. However, this process, although relatively well-controlled and straightforward, could induce the formation of structural defects[11]. The explosion and implosion of microbubbles mainly drive the exfoliation of layered materials through ultrasonication, *i.e*., phenomena known as cavitation[19–22]. Cavitation creates drastic and punctual changes of pressure, temperature and shear forces, which promote the exfoliation[19–21]. Additionally, exposure to cavitation induces structural atomic vacancies, edge defects and the formation of B-OH species[23,24].

Several theoretical models have been developed to explain the correlation between emission and defects[25–28]. A defect-free *h*-BN crystal does not display visible emission and present a sharp band-to-band absorption edge[11]. On the contrary, defective structures show interesting fluorescence properties[11]. Point defects, for instance, exhibit single-photon emission; the discovery of this property has triggered intensive research effort to design quantum emitters in a wide range of energies[29,30]. Full comprehension of the wide intragap emission observed experimentally in 2D *h*-BN materials is, however, still lacking. Therefore, we have tried to tailor defects in sonication-assisted liquid exfoliated *h*-BNNs via oxidation. Additionally, a relationship between optical properties and defects has been established based on the experimental data and quantum chemical calculations. This study provides new insights into the defect-emission relationship, underlying the impact of post-synthesis process in the optical properties of *h*-BNNs, pivotal for future applications in photonics and optoelectronics.

2. Results and discussion

Visible PL under UV excitation arises in water-assisted exfoliated *h*-BN after ultrasonication. The luminescence has been observed only if the liquid exfoliation medium is water. In fact, the exfoliation by dimethyl sulfoxide (DMSO) or N-methyl-2-pyrrolidone (NMP) has not produced fluorescent *h*-BNNs (*vide infra*). Furthermore, the new optical features in the samples exfoliated by water resulted in depending on the thermal treatment in air. The as-prepared *h*-BNN samples have been oxidized at increasing temperatures to correlate the defects with the optical properties. Different techniques have been used to detect possible changes in the material structure.

The morphology of the as-obtained materials by liquid exfoliation has been studied by TEM and HRTEM (**Figure 1)**. After exfoliation, the *h*-BNNs present a lateral size in the range of hundreds of nanometers (**Figure 1a**). No significant changes in morphology and size have been observed in the *h*-BNNs upon thermal treatment. **Figure 1 (a-c)** shows representative images of the as-obtained samples and after thermal treatments at 300 and 700 °C.

High-resolution images, **Figure 1 (d-k),** highlight the crystallinity of the nanosheets; the detected interplanar distances are in agreement with a bulk *h*-BN structure (PDF Card 34-421). After treatment at 700°C, a crystalline *h*-BNN hexagonal structure is still detected, confirming that at this temperature the *h*-BNNs do not degrade. In particular, interplanar spacings at ~2.1 Å and ~3.4 Å associated to (10–10) and to (0002) planes respectively are detected in *h*-BNN[31].

Raman spectroscopy measurements on *h*-BNNs have been performed to acquire information on the structural properties after the ultrasonic treatment (**Figure 2**) [32,33]. The *h*-BN bulk crystals show a characteristic mode at 1365.7 cm^{-1} corresponding to the E_{2g} vibration mode in *h*-BN (G band) [34,35]. The G mode band of the exfoliated *h*-BNNs is at 1367.0 cm^{-1}, in agreement with literature, suggesting a reduction of the *h*-BNN thickness corresponding to flakes with no more than three layers[35,36]. Moreover, the heat treatment at 300°C introduces a band widening that can be correlated to the decrease of B-OH, in agreement with FTIR analysis (*vide infra*). Raman spectra in a full range of temperatures are shown in **Figure S1**. Similar results have been reported by Li *et al*., for BN nanosheets, which displayed a marked upshift and widening of the G band as a function of the oxidation temperature [36].

The presence of functional groups on the surface or in the crystalline lattice of the exfoliated *h*-BNNs can be revealed by the FTIR analysis. **Figure 3** shows the FTIR absorption spectra of the as-prepared *h*-BNNs, and after thermal treatments at 100, 300, 500 and 700°C. The infrared spectra, for the sake of clarity, has been divided into five regions according to the detected vibrational modes. The region I, at higher wavenumbers, 3700 – 2800 cm^{-1}, is characterized by a broad absorption band assigned to O-H stretching[37,38]. This band is formed by two overlapped components, one peaking around 3250 cm^{-1} and another one at 3400 cm^{-1}[39]. The lower wavenumber component is due to O-H stretching in adsorbed water and the second one at 3400 cm^{-1} to O-H stretching in boron hydroxide species, B-OH. The O-H bands decrease in intensity as a function of the thermal treatment (*vide infra*).

In II and IV regions, the absorption bands at 1374 and 806 cm^{-1} are assigned to the in-plane stretching B-N vibration and the out-of-plane B-N-B bending mode, respectively[40]. The thermal treatment causes a narrowing of the Full Width at Half Maximum (FWHM) B-N vibrational mode. The intermediate region III (1180 – 840 cm^{-1}) is characterized by a broad absorption band assigned to N-B-O bands, [14,41] which increases in intensity with the thermal treatment and reaches a maximum at 700°C.

The FTIR data show a specific trend with the rise of temperature treatment: the high wavenumber band of B-OH decreases (vide infra) and correspondingly, the intensity of N-B-O increases. This trend suggests a strong correlation between hydroxyl groups and N-B-O vibrational features. In light of this, B-OH groups tend to oxidize into N-B-O structures. Interestingly, when the temperature is up to 500 and 700°C, a new absorption band at 460 cm^{-1} is detected. The latter can be attributed to O-B-O bonds, suggesting that N-B-O is oxidized into boroxyl ring.

A detailed study of O-H stretching bands (region I, **Figure 3**) has been performed by acquiring *in-situ* the absorption spectra during the heating process in step of 50°C and up to 250°C (**Figure 4**). The FTIR spectra have been deconvoluted using two Gaussian components. The two bands decrease in intensity and are difficult to detect at 200°C. The B-OH band at 3453 cm^{-1}, shifts to higher wavenumbers, which indicates a decrease in the number of H-bonded molecules. At higher temperatures, the B-OH should be mostly present as isolated or twin species. The absorption band at 3240 cm^{-1} is assigned to adsorbed water and follows the same trend as the B-OH band.

The FTIR data of *h*-BNNs as a function of the thermal treatment have been coupled with the DTA-TGA data in **Figure 5**. The DTA curve shows three endothermic events: a first drying step from 25 to 90°C associated to the loss of adsorbed water, and 0.81% weight decrease, a second one from 90 to 130°C with a 1.33% weight loss of intercalated water, and a third step from 130 up to 300°C due to B-OH condensation (1.03% weight lost). The FTIR-TGA-DTA data show that the thermal treatment at temperatures lower than 300°C produces a structural change, which is associated with a condensation process of B-OH. At higher temperatures (*i.e.*, > 300°C), the oxidation produces a second structural change with the progressive formation of boroxyl rings.

The surface composition of the *h*-BNN samples has been estimated from the area of the B 1s, C 1s, N 1s and O 1s XPS regions (see **Figure S2**) and taking into account their corresponding sensitivity factors. The results are summarized in **Table 1**. The small amount of carbon detected in the analysis can be attributed to adventitious carbon since it is a constant value. The B:N ratio in the *h*-BN bulk and the as-prepared *h*-BNNs sample are in good agreement. Both samples show a small excess of nitrogen with respect to boron and the presence of oxygen. As expected, the thermal treatments result in an increase of the amount of oxygen, and a change in the atomic B:N ratio. A gradual decrease of boron and increase of nitrogen is observed as the temperature enhances. This change rises in the samples treated at 500 and 700°C, experimenting a deficit of boron content in the B:N ratios, *i.e.*, 1:1.47 and 1:1.7, respectively.

Figure 6a shows the UV-Vis absorption spectra of the *h*-BNNs samples. The spectra are characterized by an intense absorption band in the UV region, peaking at 205 nm.

This absorption band is assigned to the *h*-BN band-to-band transition. The absorption spectra change shape with the increase of the oxidation temperature. A broad continuous band, extending from UV down to visible range, increases in intensity with the thermal treatment temperature. The bandgaps (E_g) have been calculated by the TAUC method [42–44] according to the UV-Vis absorption curves (see **Figure 6b**). The E_g shifts to a lower value, from 5.61 to 5.01 eV, with the increase of thermal treatment temperature (see inset in **Fig. 6b**). This effect can be linked with the increase of oxygen content in the *h*-BN structure [30,45].

Figure 7 shows the 3D excitation-emission-intensity spectra of *h*-BNNs in aqueous solutions. Photoluminescence of bulk *h*-BN is shown as reference in **Figure 7a**. The corresponding 2D PL spectra are reported in **Figure S3**. The bulk *h*-BN does not emit under excitation higher than 200 nm, whilst the as-prepared *h*-BNNs exhibits a blue emission with the maxima centered at λ_{ex} = 325 nm and λ_{em} = 400 nm. The sample treated at 100 and 300°C, show an increase of PL intensity from 4.5×10^5 (as prepared sample) to 5.0×10^5 (100°C) and 9.0×10^5 (500°C) counts. As reported in **Figure 3**, at the temperatures between 100 and 200 °C, the content of N-B-O bonds changes, supporting the hypothesis that the presence of N-B-O defects is strictly connected with the rise of the luminescence from 2D *h*-BN [46]. The PL goes through a maximum after the thermal treatment at 300°C and then decreases. This is because the basic *h*-BN structure with oxygen-containing defects changes with the temperature and the N-B-O are further transformed into boroxyl rings (**Figure 3**).

To demonstrate the importance of defects generated during the sonication process, and the following oxidation through the heat treatment, the vibrational and optical properties of water- and NMP-derived *h*-BNNs systems have been investigated. 3D PL spectra of the *as-prepared* water-derived *h*-BNNs sample before and after the heat treatment at 300 °C are shown in **Figure 7b** and **7d**, while the reference spectra of the NMP-derived *h*-BNNs samples with a defective structure are shown in **Figure 8a** and **8b**. *h*-BNNs without oxygen defects do not emit even after the oxidation treatment in air, demonstrating a thermal stability (more information about NMP- derived *h*-BNNs is shown in **Figure S4**). The FTIR spectra in **Figure 9a** clearly show that the increase of N-B-O content with the rise of temperature is correlated with the transformation reaction of B-OH. Additionally, the pristine *h*-BNNs samples do not show any infrared absorption in the O-H stretching range. No signals that could be correlated with the N-B-O or B-O vibrational modes are observed (**Figure 9b**). It should be underlined that weak luminescence in the as-prepared samples has been observed only in samples exfoliated in water. Samples obtained using DMSO (see **Figure S5**) or NMP have not shown the presence of OH defects and are not luminescent even after the thermal treatments.

Figure 10 shows the profile of PL decay at λ_{ex} = 300 nm. A two-exponential decay law can be applied to all the samples treated at different temperatures. The decays correspond to lifetimes of 2 and 10 ns without any detectable change in the different samples. This peculiar luminescence response is due to the presence of a single type of defects, which excludes a distribution of vacancies and impurities originated from different structural environments or possible contaminations. These results agree with

the steady-state PL, which has revealed that the thermal treatment contributes to an increase in the number of defects (growth of PL intensity), without affecting the intrinsic nature of *h*-BN defects**. Scheme 1** illustrates a possible explanation concerning the origin of the *h*-BNNs PL. At low temperature fluorescent N-B-O defects contribute to the BN visible emission. These defects are unstable at higher temperature and undergo a further oxidizing process that quenches the luminescence. On the contrary, defects free *h*-BNNs sheets have no emissions.

To better understand the properties of exfoliated *h*-BN, DFT calculations have been performed on clusters with different structural defects and the corresponding absorption properties have been derived. As a starting point, four clusters have been evaluated as the number of *h*-BN rings increased (**Table S1**). Among the different structures, we have selected the one with 19 *h*-BN rings, considered as a good compromise between the cost of the calculation and agreement with the experimental data.

It has been reported that the bandgap of the *h*-BN bulk is around 6 eV, while the one of the *h*-BN monolayer is around 5.95 eV. In our case, the bandgap has been calculated by applying the TAUC equation for an indirect bandgap system to the absorption spectra. The lower values, compared to those reported in literature [11], have been attributed to a structure with a high concentration of defects as a result of ultrasonic exfoliation treatment. In the following, we will consider intrinsic vacancies and oxygen impurities as the primary source of defects.

Defect-free BN clusters ($B_{27}N_{27}H_{18}$) show a first intense optical transition at 6.02 eV (206 nm, f = 0.33) and a second one at 6.26 eV (198 nm, f = 0.39) (**Table S1**). According to the relaxed structure, the B-N bond length is 1.45 Å at the centre of the cluster, diminishing to 1.43 Å at the edge. The defect formation energies are calculated applying the method well-grounded for supercell approach [47,48] and further implemented for cluster systems as in the present case[49], according to the following equation:

$$E_{form} = E_D(q) - E_{BN} + n_i\mu_i + q(E_{VBM} + E_F) \quad (1)$$

in which $E_D(q)$ is the defective cluster energy with charge state q, E_{BN} is the pristine *h*-BN cluster energy, n_i is the number of exchanged species and μ_i the chemical potential of the corresponding reservoir. E_F is the Fermi level referred to the energy of the maximum of the valence band (E_{VBM}), which corresponds to the highest occupied molecular energy (HOMO) state in our case.

The absorption of some defects that typically occur in *h*-BN bulk and nanosheets structures has been calculated to verify the effects of oxygen inclusions in the *h*-BN structure. Many of these defects have been studied mostly by applying the DFT method to supercell bulk systems. Rare are the cases of application on *h*-BN cluster systems. A summary of the theoretical UV-Vis spectra related to the different types of defects is shown in the **Figure 11**. The most likely defects comprise boron and nitrogen vacancies (V_B and V_N), one or two oxygen impurities on nitrogen sites O_N and $2O_N$ (oxygen on boron site has large formation energy and is unlikely to occur[47]) and oxygen inclusion on nitrogen site near a boron vacancy O_NV_B. Among these, it has been possible to select

some of the most probable defects according to the formation energy here calculated and the ones reported in previous works[30,47,48]. Despite the intrinsic difficulty of cluster model to deal with charged defects as compared to supercell approach, the data reported in **Table S2** for neutral states agree quite well with literature in predicting, in particular, that substitutional oxygen on nitrogen sites can be easily incorporated into the *h*-BN structure, possibly paired with a boron vacancy[47,48,50]. As shown in **Figure 11**, oxygen impurities are responsible for a redshift of band-to-band absorption. Furthermore, in the range between 250 nm and 500 nm (inset of **Figure 11**) several intragap transitions are appreciable. Correspondingly, a significant lowering of HOMO-LUMO energy gap as a function of defect type and charge is produced (**Table 2**). Since the formation energy can be highly dependent on the impurities electronic states, we have also examined the effects of charged defects on the optical properties. A complete investigation of *h*-BN defects is reported in **Table S3**.

Table 3 reports the HOMO and LUMO representation of the computed defects. It turns out that some point-defects undergo different mechanism under excitation, depending on the typology and charge. As an example, charged (q = +1) oxygen impurity (OB_3) can act as withdrawing sites under HOMO-to-LUMO excitation, while $2O_N$ and O_NV_B complex work as recombination centers.

Despite the intrinsic difficulty to accurately represent the impact of oxygen defect by cluster methodology, the introduction of specific defects and charges inside the nanosheets allows for a significant modulation of energy gap that, in turn, is responsible for the UV-Vis features after thermal treatments.

3. Conclusions

Defective hexagonal boron nitride nanosheets (*h*-BNNs) have been produced by ultrasonication-assisted liquid-phase exfoliation in water. The exfoliated *h*-BNNs show a broad fluorescent emission in the visible range. The thermal treatment has demonstrated to induce more structural defects on the *h*-BNNs structure, increasing the fluorescent emission. The emission has a strong dependence on heat treatment in air, with an unexpected non-monotonic trend. In particular, the fluorescence has a maximum intensity in samples oxidized at ~300 °C and decreases as the temperature increases. A study of the vibrational properties with infrared spectroscopy has revealed a close correlation between the presence of hydroxyl groups in the structure, which decreases as a function of the thermal treatment due to marked oxidation process in air. A comparison with *h*-BNNs samples exfoliated in different liquids, *i.e.* DMSO and NMP, reveals that the luminescence in the visible range depends on the nature of the defects originating during the synthesis. Theoretical calculations have supported the results, *i.e.,* the UV-Vis absorption spectra of *h*-BN cluster models with structural defects (nitrogen and boron vacancies, and oxygen impurities) have been computationally derived. Charged oxygen defects are the most promising candidates for the interpretation of the optical properties of defective *h*-BNNs, introducing intragap transitions in absorption that effectively reproduce the experimental spectra.

This study represents a further step towards a full understanding of the properties of *h*-BN layers. Structural defects, already present after synthesis, can have an

unpredictable trend in post-synthesis treatment conditions. In this scenario, an in-depth study of the effects of temperature as a function of the environment and the impurities originated in the growth process, becomes of fundamental importance for the enhancement of luminescence caused by point defects, and the increase of their stability, crucial parameters for the engineering of the *h*-BN materials for future applications in photonics and optoelectronics.

4. Experimental Section

Chemicals

Hexagonal boron nitride powder (h-BN, 99.5%, Alfa Aesar) was used as precursor; dimethyl sulfoxide (DMSO) (Sigma Aldrich), N-methyl-2-pyrrolidone (NMP) (Merk) and deionized water as liquid exfoliation media.

Preparation of h-BNNs

h-BNNs were prepared by liquid assisted exfoliation methods.

Water assisted liquid exfoliation has been carried out by dispersing *h*-BN (20 mg) powders in water (20 mL), and then seling the dispersion in a glass vial (capacity 25 mL). After 15 h sonication, the mixtures were centrifuged at 8000 rpm for 10 min, and h-BNNSs were collected from the supernatant. Immediately after, the supernatant (5 mL) was dried in a porcelain crucible (capacity 15 mL) at 60 °C. Then, the sample was thermally treated for 1 h in air at 100 °C. After cooling down to 25°C the powders could were collected for the characterizations. Water (5 mL) was poured into the crucible, and the dispersion used for spectral analysis after 10 min sonication.

DMSO assisted liquid exfoliation has been realized usig a similar method. *h*-BN (20 mg) powders were dispersed in DMSO (20 mL), and then were sealed in a glass vial (capacity 25 mL). After 15 h sonication, the mixtures were centrifuged at 3000 rpm for 10 min to precipitate the unexfoliated h-BN. Then the supernatant containing the nanosheets was centrifuged at 9500 rpm for 10 min to remove the DMSO solvent. After drying, h-BNNSs were used for the characterizations.

In the third method NMP was employed for achieving liquid assisted exfoliation. 100 mg of bulk *h*-BN were poured in 100 mL of NMP, and dispersed using a sonic bath for 6 hours. Immediately after the ultra-sonic treatment, the dispersion was centrifuged at 3000 *g* and the supernatant carefully collected by pipetting.

Oxidation thermal treatments were carried out in air at different temperatures, 300, 500, and 700 °C.

Characterization methods

UV-Vis spectroscopy was measured by a Nicolet Evolution 300 UV-Vis spectrophotometer (Thermo Fisher) with a bandwidth of 1.5 nm.

Fluorescence spectra were recorded by a “Fluoromax-3” spectrofluorometer (Horiba Jobin Yvon).

Time resolved photoluminescence (TR-PL) measurements were recorded by exciting the samples with 200 fs long pulses delivered by an optical parametric amplifier (Light Conversion TOPAS-C) pumped by a regenerative Ti:sapphire amplifier (Coherent Libra-HE). The repetition frequency was 1 kHz and the PL signal was recovered by a

streak camera (Hamamatsu C10910) equipped with a grating spectrometer (Princeton Instruments Acton SpectraPro SP-2300).

Fourier-transform infrared spectroscopy (FTIR) analysis was performed with sample powders in a potassium bromide (KBr, IR 99%, Sigma) using infrared Vertex 70v interferometer (Bruker). The baselines were fitted by a concave rubber band correction with OPUS 7.0 software; the spectra were normalized for comparison.

Thermal gravimetric analysis (TGA) was measured from room temperature to 700 °C with 5 °C min^{-1} of ramp rate under nitrogen flow of 20 mL min^{-1} by an SDT-Q600 instrument (TA Instruments).

X-ray photoemission spectroscopy (XPS) data were acquaired in a custom designed UHV system equipped with an EA 125 Omicron electron analyzer with five channeltrons, working at a base pressure of 10^{-10} mbar. Core level photoemission spectra (B 1s, C 1s, N 1s and O 1s regions) were collected in normal emission at room temperature with a non-monochromatized Al K_α X-ray source (1486.7 eV) and using 0.1 eV steps, 0.5 s collection time and 20 eV pass energy.

Raman spectroscopy measurements were performed in air at room temperature by using a triple spectrometer Jobin-Yvon Dilor integrated system and liquid nitrogen cooled charge couples-device detector. All the spectra were collected with low power excitation (lower than 5 mW) concentrated in a spot of 1 mm^2. The measurements were obtained in back scattering geometry with excitation wavelength at 532 nm generated by a a second harmonic of a Nd:YAG laser.

Transmission Electron Microscopy (TEM) in both conventional and high resolution mode was performed on a Jeol JEM 1400 Plus and Jeol JEM 2010 microscope, respectively. The samples were prepared by dispersing the sample in a tiny amount of n-octane; the dispersion was drop casted on a holey carbon-coated copper grid and let evaporate at room temperature.

Quantum chemical calculations

The optical and structural properties of boron nitride monolayers have been investigated using density functional theory (DFT). A cluster-based approach was employed to interpret the experimental data derived from large monolayers. In this context, *h*-BN clusters of different sizes were first used as a model for a defect-free system. The corresponding absorption properties were derived and compared with the experimental data. The cluster with the best compromise between calculation cost and agreement with the experimental data was chosen for further calculations. In it, some native structural defects were introduced, including boron and nitrogen vacations, and oxygen substitution defects. All of the calculations were carried out using Gaussian 16 code[51]. The energy calculations of the optimized structures were performed within density functional theory (DFT) with Becke's three parameters and the Lee−Yang−Parr's nonlocal correlation functional (B3LYP)[52,53]. The basis sets for B, N, O, and H were 6-31G(d,p), while the electronic excitation energies were calculated based on the time-dependent (TD)-DFT method. The calculations were performed using vacuum as the medium. GaussView 6 was used to interpret the computed data[54]. TD-DFT calculations were carried out on relaxed structures.

Acknowledgments
The Italian Ministry of Foreign Affairs and International Cooperation (MAECI) is acknowledged for funding through Cooperation Project "GINGSENG" (Grant PGR05249) between Italy and China. University of Sassari is acknowledged for funding through "Fondi di Ateneo 2019". L.S. gratefully acknowledges for the financial support Programma Operativo Nazionale (PON) Ricerca e Innovazione 2014-2020-Linea 1.

References

[1] Novoselov K S, Jiang D, Schedin F, Booth T J, Khotkevich V V., Morozov S V. and Geim A K 2005 Two-dimensional atomic crystals *Proc. Natl. Acad. Sci. U. S. A.* **102** 10451–3

[2] Watanabe K, Taniguchi T and Kanda H 2004 Direct-bandgap properties and evidence for ultraviolet lasing of hexagonal boron nitride single crystal *Nat. Mater.* **3** 404–9

[3] Cassabois G, Valvin P and Gil B 2016 Hexagonal boron nitride is an indirect bandgap semiconductor *Nat. Photonics* **10** 262–6

[4] Xia F, Wang H, Xiao D, Dubey M and Ramasubramaniam A 2014 Two-dimensional material nanophotonics *Nat. Photonics* **8** 899–907

[5] Tian H, Chin M L, Najmaei S, Guo Q, Xia F, Wang H and Dubey M 2016 Optoelectronic devices based on two-dimensional transition metal dichalcogenides *Nano Res.* **9** 1543–60

[6] Bonaccorso F, Sun Z, Hasan T and Ferrari A C 2010 Graphene photonics and optoelectronics *Nat. Photonics* **4** 611–22

[7] Wang Q H, Kalantar-Zadeh K, Kis A, Coleman J N and Strano M S 2012 Electronics and optoelectronics of two-dimensional transition metal dichalcogenides *Nat. Nanotechnol.* **7** 699–712

[8] Jiang, H.X.; Lin J Y 2017 Review—Hexagonal Boron Nitride Epilayers: Growth, Optical Properties and Device Applications *ECS J. Solid State Sci. Technol.* **6** 3012–21

[9] Ferreira F, Chaves A J, Peres N M R and Ribeiro R M 2019 Excitons in hexagonal boron nitride single-layer: a new platform for polaritonics in the ultraviolet *J. Opt. Soc. Am. B* **36** 674

[10] Ren J, Malfatti L, Enzo S, Carbonaro C M, Calvillo L, Granozzi G and Innocenzi P 2020 Boron oxynitride two-colour fluorescent dots and their incorporation in a hybrid organic-inorganic film *J. Colloid Interface Sci.* **560** 398–406

[11] Stagi L, Ren J and Innocenzi P 2019 From 2-D to 0-D Boron Nitride Materials, The Next Challenge *Materials (Basel).* **12** 3905

[12] Grenadier S J, Maity A, Li J, Lin J Y and Jiang H X 2018 Origin and roles of oxygen impurities in hexagonal boron nitride epilayers *Appl. Phys. Lett.* **112**

[13] Lin L, Xu Y, Zhang S, Ross I M, Ong A C M and Allwood D a. 2014 Fabrication and luminescence of monolayered boron nitride quantum dots *Small* **10** 60–5

[14] Tang C, Bando Y, Zhi C and Golberg D 2007 Boron-oxygen luminescence centres in boron-nitrogen systems *Chem. Commun.* 4599–601

[15] Ferrari A C, Bonaccorso F, Fal'ko V, Novoselov K S, Roche S, Bøggild P, Borini S, Koppens F H L, Palermo V, Pugno N, Garrido J A, Sordan R, Bianco A, Ballerini L, Prato M, Lidorikis E, Kivioja J, Marinelli C, Ryhänen T, Morpurgo A, Coleman J N, Nicolosi V, Colombo L, Fert A, Garcia-Hernandez M, Bachtold A, Schneider G F, Guinea F, Dekker C, Barbone M, Sun Z, Galiotis C, Grigorenko A N, Konstantatos G, Kis A, Katsnelson M, Vandersypen L, Loiseau A, Morandi V, Neumaier D, Treossi E, Pellegrini V, Polini M, Tredicucci A, Williams G M, Hee Hong B, Ahn J H, Min Kim J, Zirath H, Van Wees B J, Van Der Zant H, Occhipinti L, Di Matteo A, Kinloch I A, Seyller T, Quesnel E, Feng X, Teo K, Rupesinghe N, Hakonen P, Neil S R T, Tannock Q, Löfwander T and Kinaret J 2015 Science and technology roadmap for graphene, related two-dimensional crystals, and hybrid systems *Nanoscale* **7** 4598–810

[16] Zhang K, Feng Y, Wang F, Yang Z and Wang J 2017 Two dimensional hexagonal boron nitride (2D-hBN): Synthesis, properties and applications *J. Mater. Chem. C* **5** 11992–2022

[17] Bonaccorso F, Lombardo A, Hasan T, Sun Z, Colombo L and Ferrari A C 2012 Production and processing of graphene and 2d crystals *Mater. Today* **15** 564–89

[18] Bonaccorso F, Bartolotta A, Coleman J N and Backes C 2016 2D-Crystal-Based Functional Inks *Adv. Mater.* **28** 6136–66

[19] Yi M, Shen Z, Zhang X and Ma S 2012 Vessel diameter and liquid height dependent sonication-assisted production of few-layer graphene *J. Mater. Sci.* **47** 8234–44

[20] Jinzhi L, Min Y, Zhigang S, Shulin M, Xiaojing Z and Yushan X 2012 Experimental study on a designed jet cavitation device for producing two-dimensional nanosheets *Sci. China Technol. Sci.* **55** 2815–9

[21] Yi M, Shen Z and Zhu J 2014 A fluid dynamics route for producing graphene and its analogues *Chinese Sci. Bull.* **59** 1794–9

[22] Mason T J and Cintas P 2007 Sonochemistry *Handbook of Green Chemistry and Technology* pp 372–96

[23] Xiao F, Naficy S, Casillas G, Khan M H, Katkus T, Jiang L, Liu H, Li H and Huang Z 2015 Edge-Hydroxylated Boron Nitride Nanosheets as an Effective Additive to Improve the Thermal Response of Hydrogels *Adv. Mater.* **27** 7196–203

[24] Shi L, Wang D, Song W, Shao D, Zhang W P and Lu A H 2017 Edge-hydroxylated Boron Nitride for Oxidative Dehydrogenation of Propane to Propylene *ChemCatChem* **9** 1788–93

[25] Mocci P, Cardia R and Cappellini G 2019 A computational study on the electronic and optical properties of boron-nitride circumacenes *Phys. Chem. Chem. Phys.* **21** 16302–9

[26] Ravan B A and Jafari H 2019 DFT study on electronic and optical properties of halogen-adsorbed hexagonal boron nitride *Comput. Condens. Matter* **21** e00416

[27] Zunger A, Katzir A and Halperin A 1976 Optical properties of hexagonal boron nitride *Phys. Rev. B* **13** 5560–73

[28] Yamijala S S, Bandyopadhyay A and Pati S K 2013 Structural stability, electronic, magnetic, and optical properties of rectangular graphene and boron nitride quantum dots: Effects of size, substitution, and electric field *J. Phys. Chem. C* **117** 23295–304

[29] Caldwell J D, Aharonovich I, Cassabois G, Edgar J H, Gil B and Basov D N 2019 Photonics with hexagonal boron nitride *Nat. Rev. Mater.* **4** 552–67

[30] Sajid A, Reimers J R and Ford M J 2018 Defect states in hexagonal boron nitride: Assignments of observed properties and prediction of properties relevant to quantum computation *Phys. Rev. B* **97** 1–9

[31] Kim S M, Hsu A, Park M H, Chae S H, Yun S J, Lee J S, Cho D H, Fang W, Lee C, Palacios T, Dresselhaus M, Kim K K, Lee Y H and Kong J 2015 Synthesis of large-area multilayer hexagonal boron nitride for high material performance *Nat. Commun.* **6** 1

[32] Bonaccorso F, Tan P H and Ferrari A C 2013 Multiwall nanotubes, multilayers, and hybrid nanostructures: New frontiers for technology and Raman spectroscopy *ACS Nano* **7** 1838–44

[33] Ferrari A C and Basko D M 2013 Raman spectroscopy as a versatile tool for studying the properties of graphene *Nat. Nanotechnol.* **8** 235–46

[34] Cai Q, Scullion D, Falin A, Watanabe K, Taniguchi T, Chen Y, Santos E J G and Li L H 2017 Raman signature and phonon dispersion of atomically thin boron nitride *Nanoscale* **9** 3059–67

[35] Gorbachev R V., Riaz I, Nair R R, Jalil R, Britnell L, Belle B D, Hill E W, Novoselov K S, Watanabe K, Taniguchi T, Geim A K and Blake P 2011 Hunting for monolayer boron nitride: Optical and raman signatures *Small* **7** 465–8

[36] Li L H, Cervenka J, Watanabe K, Taniguchi T and Chen Y 2014 Strong oxidation resistance of atomically thin boron nitride nanosheets *ACS Nano* **8** 1457–62

[37] Zhao G, Zhang F, Wu Y, Hao X, Wang Z and Xu X 2016 One-Step Exfoliation and Hydroxylation of Boron Nitride Nanosheets with Enhanced Optical Limiting Performance *Adv. Opt. Mater.* **4** 141–6

[38] Qu T, Yang N, Hou J, Li G, Yao Y, Zhang Q, He L, Wu D and Qu X 2017 Flame retarding epoxy composites with poly(phosphazene-: Co -bisphenol A)-coated boron nitride to improve thermal conductivity and thermal stability *RSC Adv.* **7** 6140–51

[39] Innocenzi P 2003 Infrared spectroscopy of sol-gel derived silica-based films: A spectra-microstructure overview *J. Non. Cryst. Solids* **316** 309–19

[40] Gao R, Yin L, Wang C, Qi Y, Lun N, Zhang L, Liu Y X, Kang L and Wang X 2009 High-yield synthesis of boron nitride nanosheets with strong ultraviolet *J. Phys. Chem. C* **113** 15160–5

[41] Li Q, Zheng Y, Hou X, Yang T, Liang T and Zheng J 2020 A wide range photoluminescence intensity-based temperature sensor developed with BN quantum dots and the photoluminescence mechanism *Sensors Actuators, B Chem.* **304** 127353

[42] Tauc J 1968 Optical properties and electronic structure of amorphous Ge and Si *Mater. Res. Bull.* **3** 37–46

[43] Wickramaratne D, Weston L and Van De Walle C G 2018 Monolayer to Bulk Properties of Hexagonal Boron Nitride *J. Phys. Chem. C* **122** 25524–9

[44] Bilal M, Xu W, Wang C, Wen H, Zhao X, Song D and Ding L 2020 Optoelectronic Properties of Monolayer Hexagonal Boron Nitride on Different Substrates Measured by Terahertz Time-Domain Spectroscopy *Nanomaterials* **10** 762

[45] Singh R S, Tay R Y, Chow W L, Tsang S H, Mallick G and Teo E H T 2014 Band gap effects of hexagonal boron nitride using oxygen plasma *Appl. Phys. Lett.* **104** 163101

[46] Henriques J C G, Ventura G B, Fernandes C D M and Peres N M R 2020 Optical absorption of single-layer hexagonal boron nitride in the ultraviolet *J. Phys. Condens. Matter* **32** 025304

[47] Weston L, Wickramaratne D, Mackoit M, Alkauskas a. and Van De Walle C G 2018 Native point defects and impurities in hexagonal boron nitride *Phys. Rev. B* **97** 1–13

[48] Strand J, Larcher L and Shluger A L 2020 Properties of intrinsic point defects and dimers in hexagonal boron nitride *J. Phys. Condens. Matter* **32** 055706

[49] Lin C K 2018 Theoretical study of nitrogen-doped graphene nanoflakes: Stability and spectroscopy depending on dopant types and flake sizes *J. Comput. Chem.* **39** 1387–97

[50] Huang B and Lee H 2012 Defect and impurity properties of hexagonal boron nitride: A first-principles calculation *Phys. Rev. B* **86** 1–8

[51] Frisch M J, Trucks G W, Schlegel H B, Scuseria G E, Robb M a., Cheeseman J R, Scalmani G, Barone V, Petersson G a., Nakatsuji H, Li X, Caricato M, Marenich a. V., Bloino J, Janesko B G, Gomperts R, Mennucci B, Hratchian H P, Ortiz J V., Izmaylov a. F, Sonnenberg J L, Williams, Ding F, Lipparini F, Egidi F, Goings J, Peng B, Petrone a., Henderson T, Ranasinghe D, Zakrzewski V G, Gao J, Rega N, Zheng G, Liang W, Hada M, Ehara M, Toyota K, Fukuda R, Hasegawa J, Ishida M, Nakajima T, Honda Y, Kitao O, Nakai H, Vreven T, Throssell K, Montgomery Jr. J a., Peralta J E, Ogliaro F, Bearpark M J, Heyd J J, Brothers E N, Kudin K N, Staroverov V N, Keith T a., Kobayashi R, Normand J, Raghavachari K, Rendell a. P, Burant J C, Iyengar S S, Tomasi J, Cossi M, Millam J M, Klene M, Adamo C, Cammi R, Ochterski J W, Martin R L, Morokuma K, Farkas O, Foresman J B and Fox D J G16_C01

[52] Becke A D 1993 Density-functional thermochemistry. III. The role of exact exchange *J. Chem. Phys.* **98** 5648–52

[53] Lee, Chengteh; Yang, Weitao; Parr R G 1988 Development of the Colle-Salvetti correlation-energy formula into a functional of electron density *Phys. Rev. B* **37** 785–9

[54] Dennington, Roy; Keith, Todd A.; Millam, John M. Semichem Inc., Shawnee Mission K 2016 GaussView, Version 6

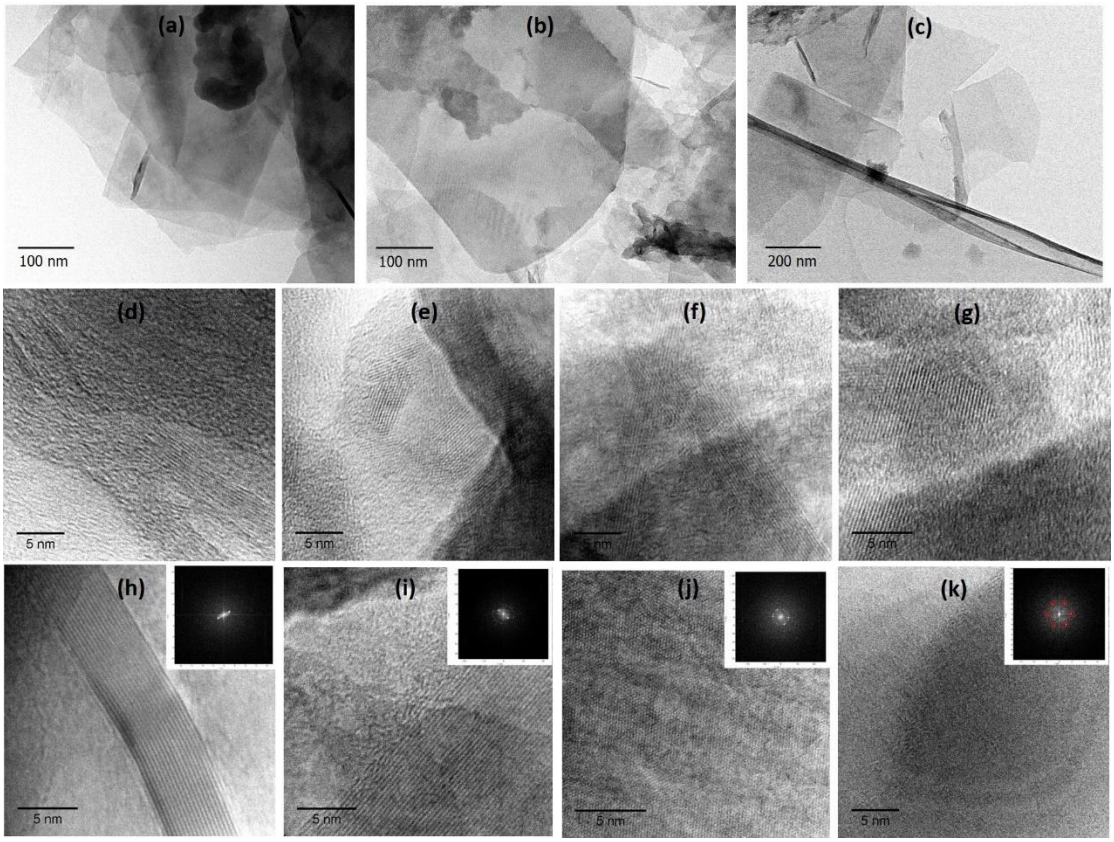

Figure 1. TEM images of as-prepared *h*-BNNs (a), after treatment at 300 (b) and 700°C (c). High resolution transmission electron microscopy images of the *h*-BNN as obtained by exfoliation (d-h) and after thermal treatment at 300 (i) and 700°C (j, k). The FFT of the images is reported as inset. The red circles in the inset of panel (k) highlight the hexagonal symmetry.

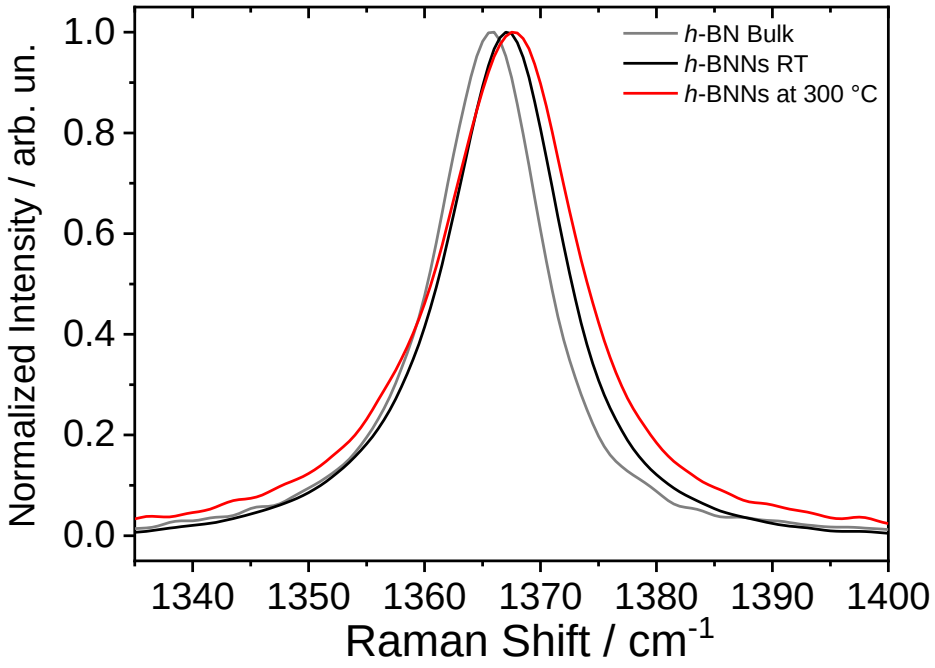

Figure 2. Raman spectra in the 1350 – 1390 cm^{-1} range of bulk *h*-BN (grey curve), exfoliated *h*-BN (black curve), exfoliated *h*-BN after thermal treatment at 300°C (red curve).

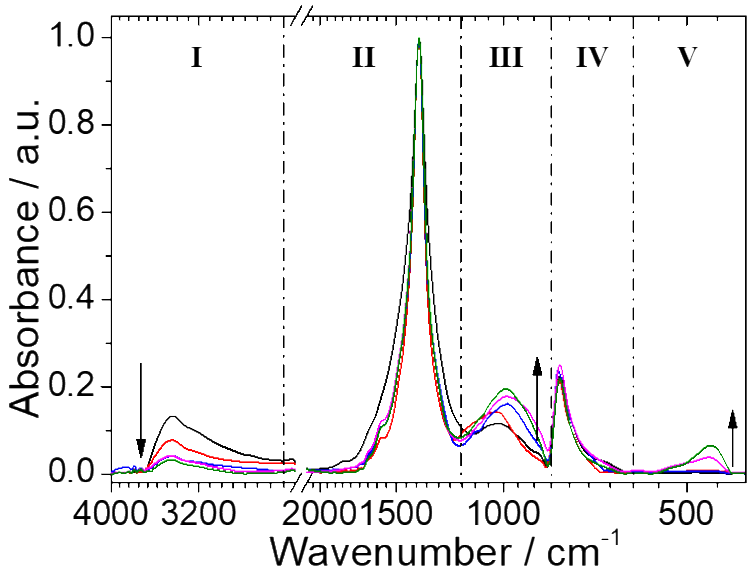

Figure 3. FTIR spectra of as-prepared *h*-BNNSs (black line) and thermally treated *h*-BNNs at 100 °C (red line), 300 °C (blue line), 500 °C (pink line), and 700 °C (green line). The spectra are divided in five regions according to the different vibrational modes. The arrows indicate the change in intensity as a function of thermal treatment; arrow up, the intensity increases with the increase of the temperature while the arrow down is the other way round.

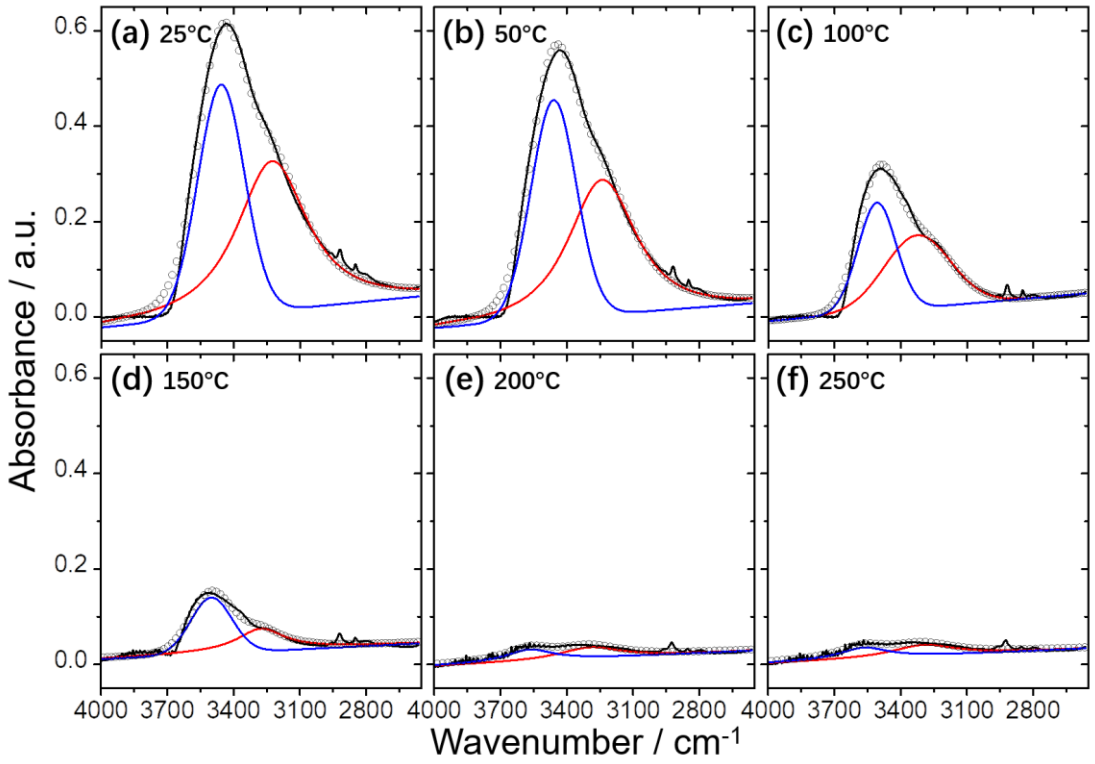

Figure 4. *In-situ* FTIR absorption spectra in the 4000 – 2500 cm^{-1} range of the as-prepared *h*-BNNs: (a) 25°C, (b) 50°C, (c) 100°C, (d) 150°C, (e) 200°C, and (f) 250°C. The black lines are the raw spectra, the dotted lines are the fitting curves, the blue and red lines are the deconvoluted components assigned to B-OH and O-H, respectively.

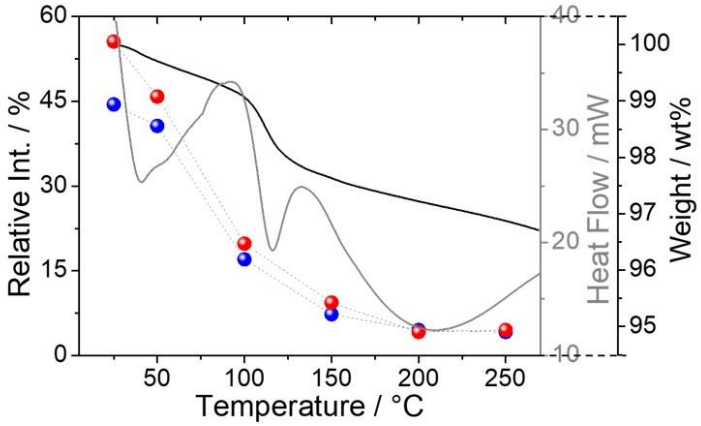

Figure 5. The relative absorption intensities of B-OH (blue dots) and O-H (red dots) bands in in-situ IR spectra as a function of temperature, coupled with TGA (black line) and heat flow (gray line) curves of the as-obtained *h*-BNNs. The lines connecting the red and blue dots are guide for eyes.

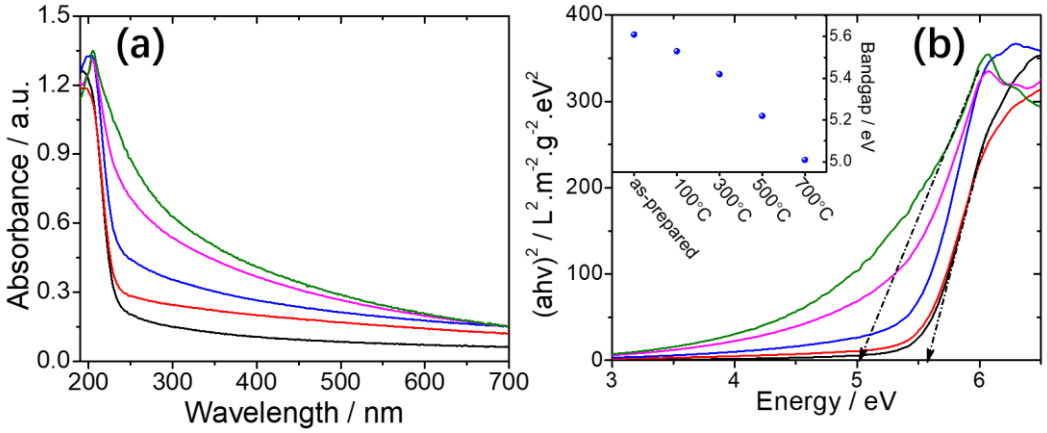

Figure 6. (a) UV-Vis absorption spectra and (b) evaluation of E_g using TAUC equation for as-prepared *h*-BNNs (black line, 5.61 eV), *h*-BNNs at 100 °C (red line, 5.53 eV), 300 °C (blue line, 5.42 eV), 500 °C (pink line, 5.22 eV), and 700 °C (green line, 5.01 eV). The insert of (b) shows the obtained E_g values.

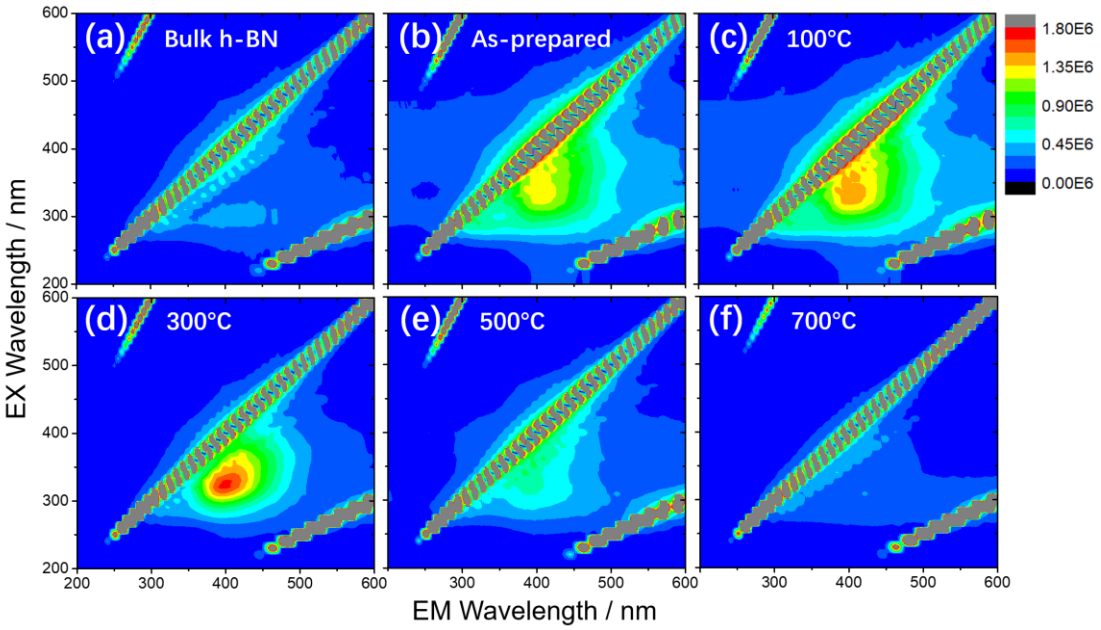

Figure 7. 3D PL excitation-emission-intensity spectra of (a) bulk *h*-BN, (b) as-prepared *h*-BNNs, (c) 100°C, (d) 300°C, (e) 500°C, and (f) 700°C. In grey: first and second order artefacts.

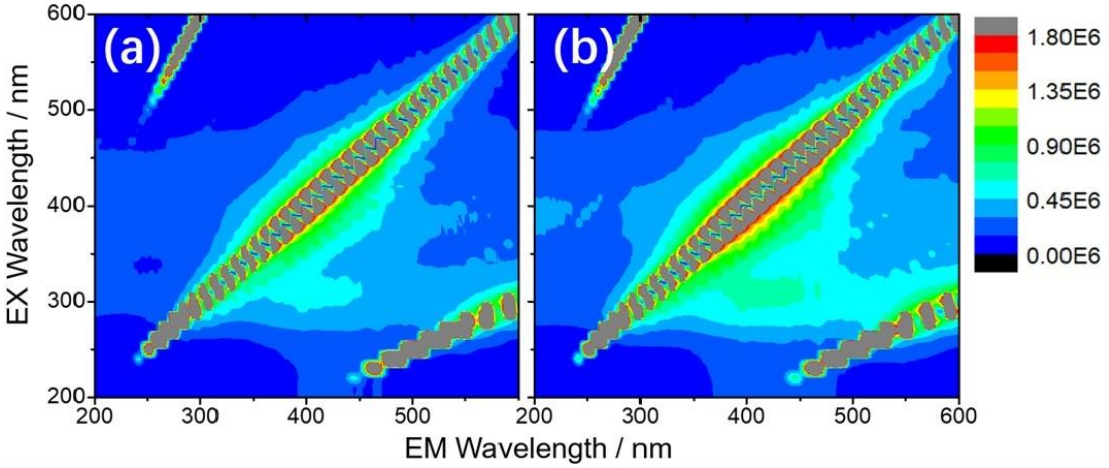

Figure 8. 3D PL excitation-emission-intensity spectra of (a) as-prepared low defects *h*-BNNs and (b) after treatment at 300°C. In grey: first and second order artefacts.

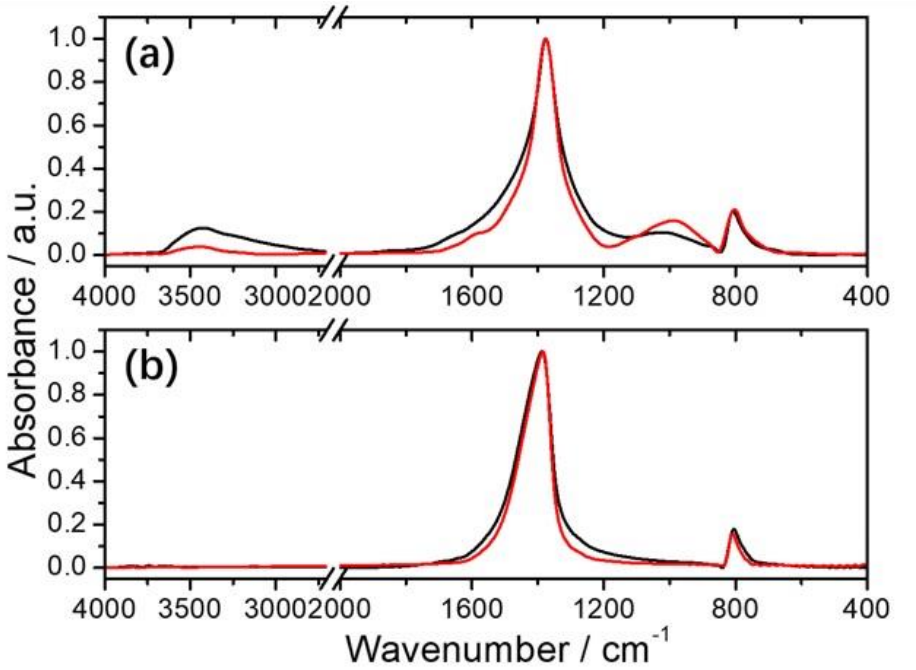

Figure 9. FTIR spectra of a) as-prepared *h*-BNNs (black line) and after thermal treatment at 300°C (red line), b) as-prepared defect-free *h*-BNNs (black line) and after thermal treatment at 300°C (red line).

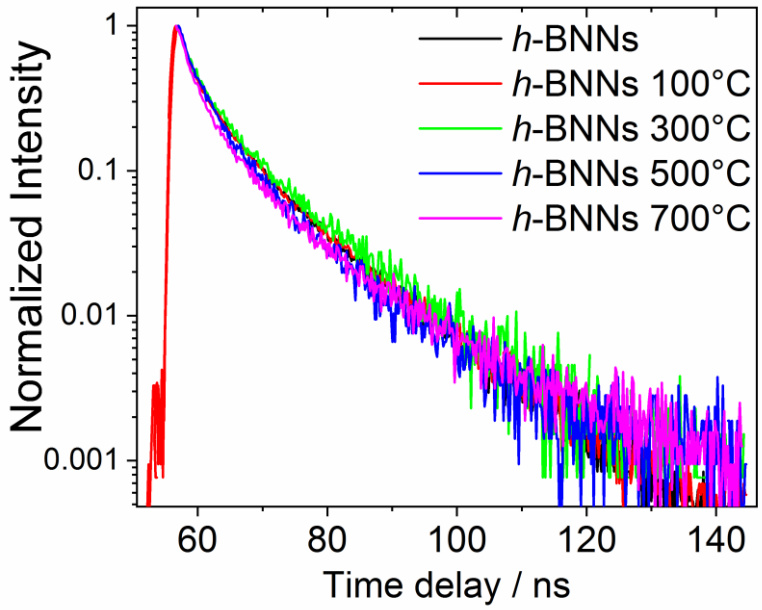

Figure 10. Time-resolved PL profile of *h*-BNNs treated at different temperatures.

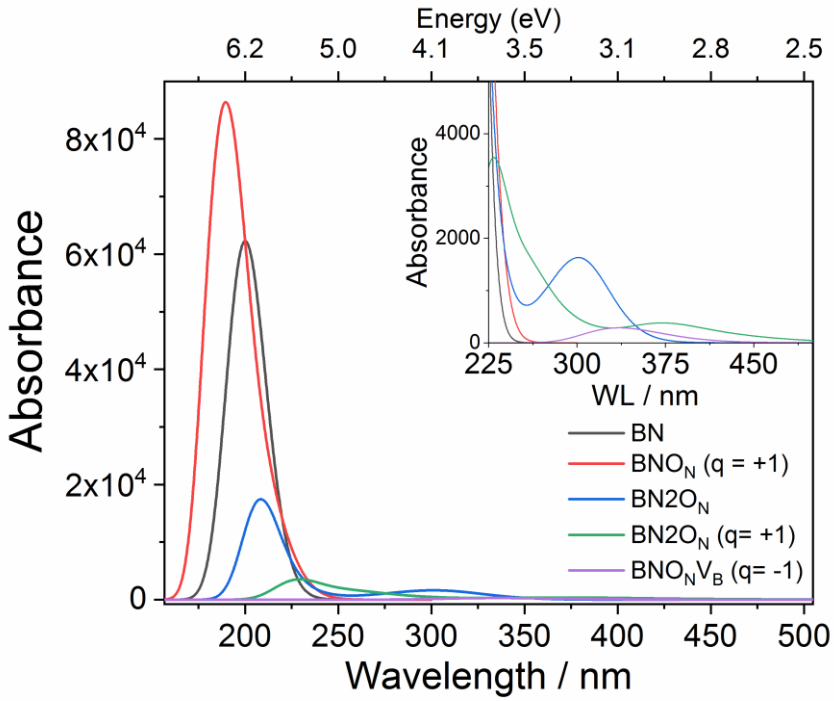

Figure 11: Computed UV-Vis absorption of pristine and defective *h*-BN clusters.

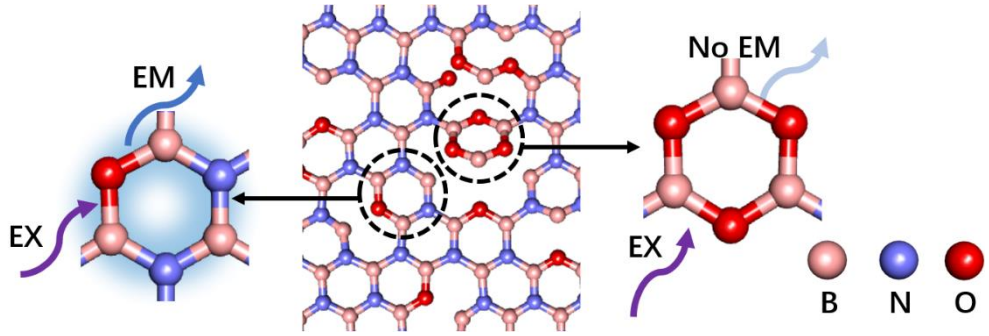

Scheme 1. Schematic illustration for a possible fluorescent origin and mechanism from *h*-BNNs.

Table 1. Surface composition of the *h*-BN samples determined from XPS.

Sample	B (at.%)	N (at.%)	C (at.%)	O (at.%)	B:N ratio
h-BN bulk	42.8	46.3	3.1	7.8	1 : 1.08
h-BNNs	42.6	44.2	2.8	10.4	1 : 1.04
h-BNNs 300 °C	37.9	41.0	3.6	17.5	1 : 1.08
h-BNNs 500 °C	35.0	51.4	2.0	11.6	1 : 1.47
h-BNNs 700 °C	29.9	50.8	3.5	15.8	1 : 1.70

Table 2: HOMO and $\Delta E_{HOMO\text{-}LUMO}$ values.

Structure /q	E_{HOMO} (eV)	$\Delta E_{HOMO\text{-}LUMO}$ (eV)
BN	-6.53	6.58
BNO_N/+1	-9.10	5.96
$BN2O_N$/0	-4.97	4.77
$BN2O_N$/+1	-6.92	3.73
$BN2O_NV_B$/-1	-1.01	3.17

Table 3: Representation of HOMO and LUMO.

Defect / Charge	HOMO	LUMO
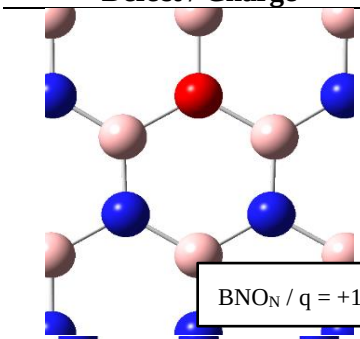 BNO_N / q = +1	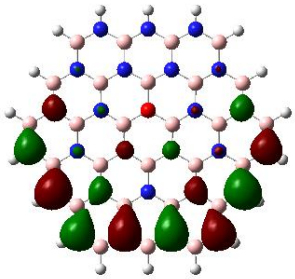	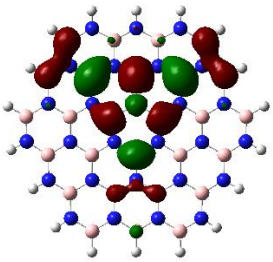
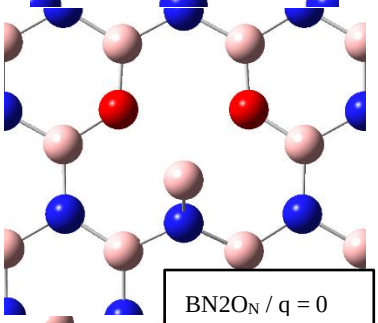 $BN2O_N$ / q = 0	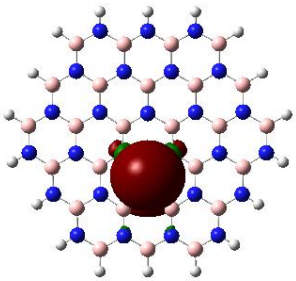	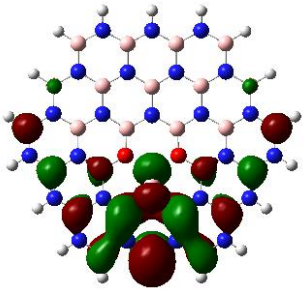
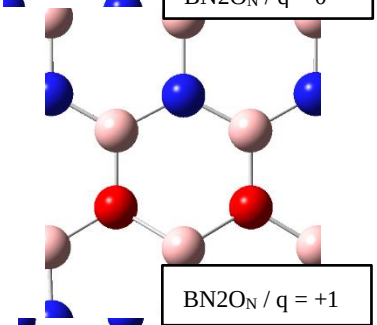 $BN2O_N$ / q = +1	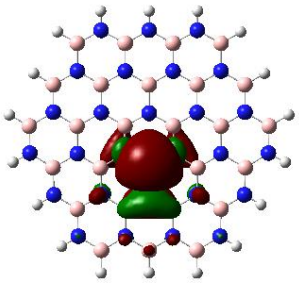	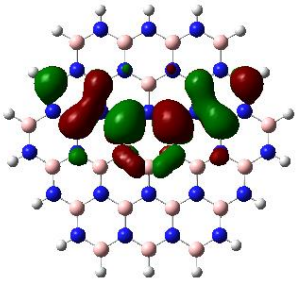
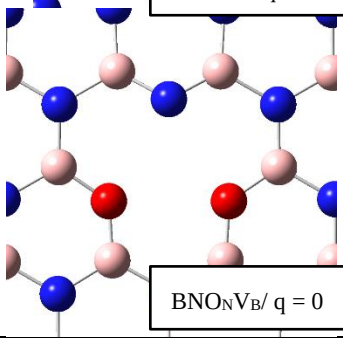 BNO_NV_B/ q = 0	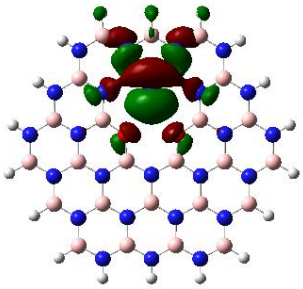	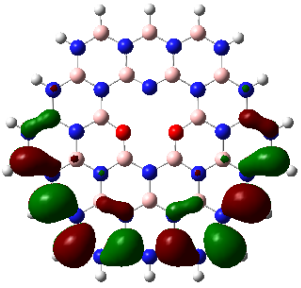

Keyword: hexagonal boron nitride

Junkai Ren, Luigi Stagi, Carlo Maria Carbonaro, Luca Malfatti, Maria Francesca Casula, Pier Carlo Ricci, Antonio Esau Del Rio Castillo, Francesco Bonaccorso, Laura Calvillo, Gaetano Granozzi, and Plinio Innocenzi*

Defect-assisted photoluminescence in hexagonal boron nitride nanosheets

ToC